International Journal of Multiphase Flow 36 (2010) 815–824

Contents lists available at ScienceDirect

International Journal of Multiphase Flow

journal homepage: www.elsevier.com/locate/ijmulflow

Planar laser-induced fluorescence (PLIF) measurements of liquid film thickness in annular flow. Part I: Methods and data

D. Schubring [a,b,*], A.C. Ashwood [b,c], T.A. Shedd [b], E.T. Hurlburt [d]

[a] Visualization, Imaging, and Computation of Thermohydraulics for Reactors (VICTR) Lab, University of Florida, 202 Nuclear Science Building, P.O. Box 118300, Gainesville, FL 32611-8300, USA
[b] Multiphase Flow Visualization and Analysis Laboratory (MFVAL), University of Wisconsin-Madison, 1500 Engineering Drive, Madison, WI 53706-1609, USA
[c] National Renewable Energy Laboratory, 1617 Cole Blvd., Golden, CO 80401, USA
[d] Bettis Laboratory, West Mifflin, PA 15122, USA

ARTICLE INFO

Article history:
Received 21 September 2009
Received in revised form 26 May 2010
Accepted 30 May 2010
Available online 8 June 2010

Keywords:
Film thickness
Vertical flow
Annular flow
Fluorescence

ABSTRACT

Most approaches to the modeling of annular flow require information regarding the thin liquid film surrounding the central gas core. This film is hypothesized to present a rough surface to the gas core, enhancing interfacial shear and pressure loss, with the roughness closely linked to the height of the film. This height is typically obtained from conductance probe measurements. The present work used planar laser-induced fluorescence to provide direct visualization of the liquid film in upward vertical air–water annular flow. Images were processed to produce the distribution of film heights. The standard deviation and average film thickness are found to be an increasing function of liquid flow and a decreasing function of gas flow, with the standard deviation approaching 0.4 times the average at sufficient liquid flow.

1. Introduction

In industrial heat transfer applications with two-phase flow, the annular regime is among those of foremost interest due to the large number of systems and wide range of flow qualities in which it is seen. This regime is characterized by the presence of a thin liquid film flowing along the walls surrounding a fast-moving gas core. Liquid droplets may travel in this core (entrainment). As observed by Hewitt et al. (1990), this film is composed of both a thin, relatively smooth base film and thicker, rougher disturbance waves. The liquid film may also contain entrained gas bubbles.

Typically, modeling of annular flow is linked to the film roughness concept, part of the triangular relationship asserted by Hewitt and Hall Taylor (1970) and others. The presence of the liquid film is modeled to present a rough surface to the gas core, enhancing the interfacial friction factor (and therefore interfacial shear and pressure loss). Film roughness is most often considered in a single zone, with the recent two-zone (base film and waves) model of Hurlburt et al. (2006) being an exception. Wallis (1969) modeled this enhancement effect as a offset linear function of average film thickness, while Asali et al. (1985), Kishore and Jayanti (2004) proposed other expressions for the roughness as a function of average film thickness. Owen and Hewitt (1987) graphically correlated the relationship between average film height and roughness.

While it is perhaps more intuitive that the enhancement of interfacial shear be linked to some parameter regarding the distribution of instantaneous film heights (e.g., standard deviation), such measurements are extremely challenging. Most measurements of film height have been taken using conductance probes (see, for example, Brown et al., 1978, Fossa, 1998, Fore et al., 2000, and, particularly, the review of Clark (2002)). Conductance probes directly measure the conductivity of a two-phase mixture. This is interpreted as a void fraction based on a calibration of the probe. In the case of annular flow (in which the gas is assumed to travel on top of a thin film), the height of that film can be estimated.

The present study proposes instead the use of an optical technique, planar laser-induced fluorescence (PLIF). A small concentration of a fluorescent dye (Rhodamine B) is introduced into the water, causing the liquid film to appear as bright regions on the images once exposed to laser light. These images are then processed to locate the edge of the bright region, asserted to be the gas–liquid interface. It should be emphasized that PLIF is not used

* Corresponding author at: Visualization, Imaging, and Computation of Thermohydraulics for Reactors (VICTR) Lab, University of Florida, 202 Nuclear Science Building, P.O. Box 118300, Gainesville, FL 32611-8300, USA. Tel.: +1 352 392 1401x314; fax: +1 352 392 3380.
E-mail address: dlschubring@ufl.edu (D. Schubring).

0301-9322/$ - see front matter © 2010 Elsevier Ltd. All rights reserved.
doi:10.1016/j.ijmultiphaseflow.2010.05.007

in this work to determine the detailed concentration of the dye (as is the case in many LIF studies), but rather its presence (indicating liquid film) or absence (indicating gas core) and using that result to estimate film height.

The immediate antecedent to this work is the dissertation of Rodríguez (2004), in which horizontal wavy-annular and annular flows were studied using a similar PLIF technique. Some of the results were also reported in Rodríguez and Shedd (2004). Using optical methods in a round tube near the wall (less than 100 μm) requires an excellent match in the index of refraction between the liquid phase (water) and the wall material. Fluorinated ethylene propylene (FEP) was selected for this purpose, as was done by Hewitt et al. (1990).

The present experimental method (with image processing) offers several advantages over the current datum (conductance probe measurements):

- *Visualization* of the thin film of annular flow is possible, since images are produced. Conductance probes produce no data beyond a time-series of conductivity (or a related parameter).
- *High axial resolution* can be obtained (on the order of 10 μm, a few times the pixel size), unlike the implicitly spatially-average conductance probe data.
- The *difference between base film and waves* can be observed directly from the images.
- *Small spatial-scale measurements*, impossible with time-series conductance probe data, can be made.
- *A more direct estimate of roughness* is made possible, due to these small spatial-scale measurements.
- Enhanced *quantification of errors* and *improvement of processing algorithms*, as the processing result can be compared to raw images. Conductance probe data are not persistent (i.e., erroneous results in conductance probe data cannot be easily identified and no re-processing is possible).
- PLIF is a *non-intrusive* method, as it does not require the installation of a probe into the flow or even flush with the inside wall of the tube.

The present paper describes the study from experiment construction to single-zone film thickness distribution, including image processing methods. The data discussed in the present paper are also used to improve the understanding and modeling of the underlying physics of annular flow, including division between base film and waves. This analysis is considered in Part II: Analysis and Comparison to Models (Schubring et al., 2010).

2. Experimental

2.1. Flow loop

The experimental facility is shown in Fig. 1. A 23.4 mm (ID) quartz test section was used for differential pressure measurements. Compressed air was run through an oil/particulate filter prior to flowing through two identical rotameters. Each had a maximum nominal volumetric flow rate ($Q_{g,nom}$) of 1400 L min^{-1} and an uncertainty of 70 L min^{-1}. One rotameter was used for all flows at or below 1200 nominal L min^{-1} and was set to read 1200 L min^{-1} for flow rates above this, with the second air controller adjusted to produce the desired nominal air flow rate. Uncertainties at and above 1400 nominal L min^{-1} are estimated at 100 L min^{-1}, based on the assumption that the measurement error in each rotameter is independent. $Q_{g,nom}$ is adjusted to actual gas mass flow rate, $\dot{m}_g$, using (as recommended by the manufacturer):

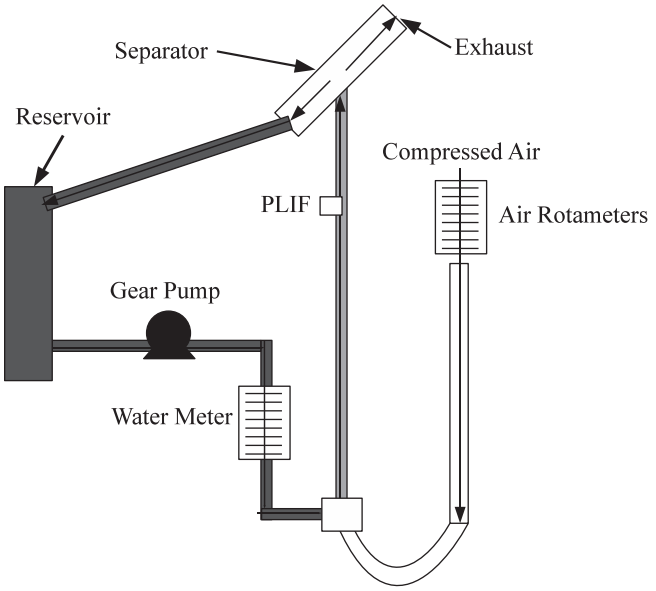

Fig. 1. Diagram of flow loop.

$$Q_{g,meter} = Q_{g,nom}\sqrt{\frac{P_{std}}{P_{meter}}} \tag{1}$$

$$\dot{m}_g = \rho_{g,meter} Q_{g,meter} \tag{2}$$

A Cole-Parmer stainless steel pressure transducer was used at the air meters to measure the local gauge pressure and to compute the absolute meter pressure, P_{meter}. Pressure data were fed to a PC through an Agilent 34790A data acquisition system. The manufacturer-specified uncertainty is 830 Pa. A standard pressure, P_{std}, of 101.35 kPa (14.7 lbf in^{-2}) was employed in Eq. (1), as recommended by the manufacturer.

City water entered a PVC reservoir through particulate and deionizing filters. Up to 8 L min^{-1} of water was provided to the loop with one of two gear pumps. Water flowed through a 200 μm filter before the pumps and an 80 μm filter after. For pressure drop and flow rate data (taken in a quartz tube), the first gear pump and a Coriolis meter with digital display and an uncertainty of 0.1% of reading was used. For the PLIF images, a second gear pump was used with a rotameter with dual (SI and US customary) readings. The manufacturer's specified uncertainty is 3% of full scale. Taking the larger of the two full scales (3 gal min^{-1}), this yields a liquid flow rate uncertainty of 0.35 L min^{-1}.

Prior to mixing, the air passed through flow straighteners beneath the loop as it turned upward. Water was introduced perpendicular to the air flow through several 2 mm holes. The two-phase mixture flowed in a 23.7 mm ID copper development length approximately 2 m long. The flow encountered a weak contraction to the quartz tube (23.4 mm) and was allowed to develop a further 1.7 m before the center of the test section.

A development length based on this location is approximately 150 L/D, although the re-development necessary after the contraction may adversely affect the degree to which the flow in the test section was developed. Based on the work of Wolf et al. (2001), film flow rate measurements (equivalent to entrainment measurements if total liquid mass flow rate is known) are the last major flow behavior to develop fully. Ishii and Mishima (1981) provide a correlated for required development length for entrained fractions, also reported by Kataoka et al. (2000). For the flows of interest, the largest L/D produced for this correlated is 160, with many less than 100. Based on these estimates, the flows are fully developed or nearly so.

For an example flow, Wolf et al. (2001) provide film thickness distributions as the flow develops (Fig. 6 in their work). The results from the present study are most similar to those for fully developed flow (the last plot), further suggesting that developing flow effects are small. Although their data indicate flow development after 150 L/D is a 10% effect, Wolf et al. (2001) suggest a development length of up to 300 L/D. As a result, the measurements in the present work may include some flow development effects; future work with the present technique will more explicitly address flow development, developing annular flow, and the effects of the method of gas–liquid mixing.

To estimate test section conditions accurately, differential pressure and absolute pressure measurements were taken. The differential measurement was taken across 0.792 m, using continuously-bled water-filled tap lines to avoid the presence of a two-phase mixture in the tap lines A Yokogawa EJA110A differential pressure transmitter was employed to provide data to the Agilent DAQ. The repeatability of differential pressure measurements on different days was 5%, which may involve imprecisions in the repeatability of flow rates and changing temperatures. By propagating meter and statistical uncertainties for a specific measurement, an uncertainty of 150 Pa m^{-1} is estimated. The total uncertainty of the pressure gradient measurements is therefore estimated at 5–10%.

The upstream pressure tap was also used for an absolute pressure measurement, taken using the same type of equipment as the measurement at the air meter. Flow rates and fluid properties were evaluated based on this absolute pressure less half the differential pressure found. Considering all sources of uncertainty regarding flow rates and pressures, typical total uncertainties for superficial velocities, U_{sg} and U_{sl}, are estimated as 10–15% and 5%, respectively. Superficial velocities are defined by:

$$U_{sg} = \frac{\dot{m}_g}{\rho_g A} \tag{3}$$

$$U_{sl} = \frac{\dot{m}_l}{\rho_l A} \tag{4}$$

With $\dot{m}_g$ and $\dot{m}_l$ as the gas and liquid mass flow rates, ρ_g and ρ_l the gas and liquid densities in the test section, and A the test section flow area. In annular flow, the superficial gas velocity, U_{sg}, is a good first approximation for the average physical velocity since the void fraction is close to one.

After the test section, the two-phase mixture encountered a separator, mounted at a 45° angle from the test section, to assist in liquid recovery. A type T thermocouple was placed in this separator to estimate test section temperature. Water was returned to the reservoir, while air was removed from the laboratory through an exhaust duct.

The flow facility was modified for PLIF measurements to include a 22.4 mm ID fluorinated ethylene propylene (FEP) test section. This test section is slightly smaller than the quartz tube (23.4 mm ID) used for pressure and flow rate measurements. The adjustment to these data is discussed in Section 2.4. The last 1.25 m of the quartz test section was replaced with FEP. The total development length is therefore unchanged, but the flow in the FEP facility encountered an additional weak contraction approximately 55 L/D upstream of the test section.

An FEP tube was selected due to the similarity of its index of refraction (1.337) with that of water at typical test section temperatures (1.333–1.334 for temperatures of 9–15 °C). This excellent match reduces the distance for which strong distortion effects are present to a dark area in the images approximately 40 μm in thickness. Since typical film heights are on the order of 100 μm, this dark area does not adversely affect identification of the gas–liquid interface. In contrast, the difference in indices of refraction of water and quartz (1.5) would produce a distorted region as large as 1 mm; essentially all of the film would be obscured.

2.2. PLIF optics

PLIF measurements use a fluorescing material within the liquid phase, a monochromatic laser light, and a camera for observation of the resulting fluorescence. Rhodamine B dye was introduced into the liquid phase to produce visible fluorescence. This dye tints the water pink or red depending on concentration, absorbs light maximally at 545 nm, and emits light maximally at 565 nm. At very high concentrations, Rhodamine B dye acts as a surfactant, indicating that the surface tension is affected by the concentration of this dye. This reduction in surface tension may directly affect film height and may also increase the number of bubbles (particularly small bubbles) entrained within the liquid film. The minimum amount of dye required to produce acceptable images was selected; based on the volume and concentration dye injected and the total volume of water in flow loop, a dye concentration of 200 mg L^{-1} is estimated.

A schematic of the test section and optics are shown in Fig. 2. The FEP tube was surrounded by a square, water-filled enclosure to ensure that light (from the laser or fluorescent dye) only passed through a large index of refraction step (air–water or air–FEP) at a right angle. The enclosure was painted black and used to surround the test section to minimize background light (i.e., light from sources other than the laser), improving the contrast of resulting images. The laser and camera were placed 90° apart around the tube to allow for cross-sectional viewing of the film, with viewing windows provided to allow light to pass. The laser was used to form a light sheet, allowing investigation of a small portion of the liquid film. The camera was then focused on this light sheet to minimize the effects from out-of-plane features. Based on visual examination of processed images, highly accurate focus (to within approximately 10 μm) was required to produce optimal edge detection. It is not immediately clear why the range of best focus is so much smaller than the nominal depth of field of the lens used.

A 1 mm thick laser sheet was produced by a New Wave Research Solo PIV Nd:YAG laser (532 nm) with a commercial light sheet attachment. A Roper-Scientific 1300YHS-DIF camera (1300 by 1030 pixels, inter-line transfer CCD) was equipped with a microscope objective lens and placed on a rigid support. A red filter was used on the camera to ensure that fluorescence dominates the resulting images and the scattered green laser light did not contaminate the images. The lens employed (Mitutoyo Telecentric

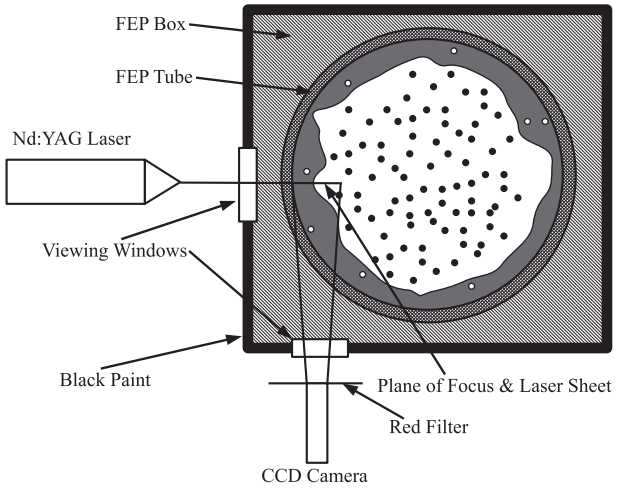

Fig. 2. Test section for PLIF measurements. Flow is out of the plane of the page.

Objective 3×, NA = 0.07, nominal working distance 72.5 mm, depth of focus 56 μm) yielded pixels 3.14 μm in each direction (4 mm total axial length).

2.3. PLIF image acquisition

A total of 400 images were taken for each flow condition. Since a dual-pulse laser was used, the images were taken as pairs to speed imaging. To ensure that the two images are independent measurements, a large time separation was used (60 ms). While for some flows this is comparable to the time between disturbance waves, no significant correlation was found between the average film thicknesses of paired images. Images were acquired in 4 batches of 100 and cropped to 500–700 pixels wide (radial direction). All images for a given flow condition were taken before proceeding to the next. The flow with U_{sg} of 84 m s^{-1} and U_{sl} of 21 cm s^{-1} includes only 300 images due to operator error in image acquisition.

2.4. Flow rate adjustment

Since the diameter of both tubes is known and water is well-modeled as incompressible, the adjustment to liquid flow rate is elementary. At the same meter reading, the same mass flow rate of liquid is introduced to the facility, leading to an increase of 9.1% on liquid superficial velocity or liquid mass flux. In contrast, air cannot be modeled with a constant density; absolute pressure and temperature data are required. The temperature in the FEP tube is assumed to be the same as that in quartz tube for the same flow condition.

Direct measurements of absolute pressure at the air meter and in the test section, along with pressure gradient in the test section, were not performed in the FEP tube. Measurements of absolute pressure at the air meter for two ducts of different internal side length (24.9 and 21.9 mm) have been performed in the facility as part of another investigation. These data indicate that the pressure at the air meter is not affected significantly by the size of the test section for the same meter readings. The separator was also unchanged between the quartz and FEP test sections, suggesting that the same absolute pressure might be present there. This absolute pressure is not known accurately, but can be expected to vary little with flow rate and to be slightly below atmospheric pressure due to the exhaust fan.

To compare pressure drops, a proportionality of pressure gradient with the product of total mass flux and gas superficial velocity divided by tube diameter was assumed. This was found to be approximately valid across a wide range of air–water flow conditions in horizontal geometry (Schubring and Shedd, 2008) and reasonable for the vertical quartz tube. Given these assumptions, a set of equations can be constructed for estimation of relevant flow rates and pressure data:

$$\dot{m}_{g,FEP} = \dot{m}_{g,Quartz} \tag{5}$$

$$G_{g,FEP} = \frac{4\dot{m}_{g,FEP}}{\pi D_{FEP}^2} \tag{6}$$

$$\rho_{g,FEP} = \rho_{g,FEP}(T, P_{abs,FEP}) \tag{7}$$

$$U_{sg,FEP} = \frac{G_{g,FEP}}{\rho_{g,FEP}} \tag{8}$$

$$\frac{dP}{dx_{FEP}}\left(\frac{dP}{dx_{Quartz}}\right)^{-1} = \frac{G_{g,FEP}U_{sg,FEP}}{D_{FEP}}\left(\frac{G_{g,Quartx}U_{sg,Quartz}}{D_{Quartz}}\right)^{-1} \tag{9}$$

$$P_{abs,FEP} = P_{separator} + \frac{dP}{dx_{FEP}}L_{eff} \tag{10}$$

$$P_{abs,Quartz} = P_{separator} + \frac{dP}{dx_{Quartz}}L_{eff} \tag{11}$$

Since all quartz data (subscripted *Quartz*), T, and D_{FEP} are known, these are a set of seven equations for eight unknowns ($\dot{m}_{g,FEP}$, $G_{g,FEP}$, $\rho_{g,FEP}$, $U_{sg,FEP}$, dP/dx_{FEP}, $P_{abs,FEP}$, L_{eff}, and $P_{separator}$) for each flow condition. Three of the unknowns refer to flow rates: $\dot{m}_{g,FEP}$, the mass flow rate of air in the FEP test section; $G_{g,FEP}$, the mass flux of air in the FEP test section; and $U_{sg,FEP}$, the gas superficial velocity in the FEP test section. One is a fluid property ($\rho_{g,FEP}$, the gas density in the test section), while three are related to pressure measurements: the absolute pressure in the FEP test section, $P_{abs,FEP}$; the absolute pressure in the separator, $P_{separator}$; and the pressure gradient in the FEP test section, dP/dx_{FEP}.

It is expected that L_{eff}, the effective length between the test section and the separator, will be similar across a wide range of flows and similar to the physical distance from the center of the test section to the separator. $P_{separator}$ is also expected to be similar across a wide range of flows. A gauge was placed at the separator to estimate this pressure; it had the same reading (to within visual uncertainty) across all flows considered. The value of $P_{separator}$ was manually iterated in a realistic range (slightly below atmospheric pressure). The best results were found with $P_{seperator}$ set to 98 kPa, producing L_{eff} results narrowly distributed around 0.45 m (similar to the corresponding physical distance). The adjusted flow rates based on this $P_{separator}$ are used in this investigation.

The total uncertainty on $P_{abs,FEP}$ (and, thus, $\rho_{g,FEP}$) is estimated at 3 kPa.

The estimated pressure gradient can then be used to approximate wall shear, $\tau_{w,FEP}$ allowing for non-dimensional (wall) coordinates to be used for radial distances y^+, including film thickness, (δ, in dimensionless form δ^+), as desired, based on the friction velocity, u^*, and the kinematic viscosity of the liquid, ν_l:

$$\tau_{w,FEP} = -\frac{D}{4}\frac{dP}{dx_{FEP}} \tag{12}$$

$$u^* = \sqrt{\frac{\tau_{w,FEP}}{\rho_l}} \tag{13}$$

$$y^+ = \frac{u^* y}{\nu_l} \tag{14}$$

$$\delta^+ = \frac{u^* \delta}{\nu_l} \tag{15}$$

3. PLIF processing

The raw images were processed using MATLAB to produce images that indicate the edge detected and are appropriate for manual investigation and to calculate film thickness distributions. The processing algorithm iterates on the height of each image to minimize the influence of non-interfacial features, such as bubbles in the film and droplets near the interface. Typical spurious results due to bubbles are also identified, further reducing this source of error. The code then post-processes the images to compute film thickness statistics.

3.1. PLIF image processing

Image are processed by the following steps. An example image processing is shown in Fig. 3. Four primary challenges must be overcome in the processing:

1. Limited brightness/contrast due to small spatial scales being studied.
2. Single-pixel noise.
3. Entrained bubbles in the film.
4. Entrained droplets in the gas and other out-of-plane features.

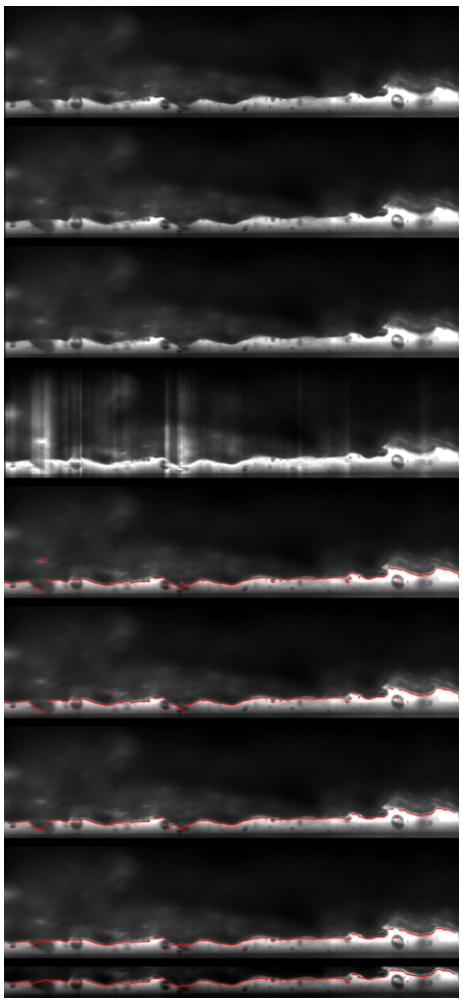

Fig. 3. Example of an image processing procedure from flow with U_{sg} = 55.3 m s^{-1} and U_{sl} = 12.7 cm s^{-1}. Flow is right to left.

1. *Crop.* The left edge of the image is selected based on the manually identified location of the wall at the vertical (axial) midpoint of the image. A misalignment of the wall (10–20 μm) is accounted for in later processing. The initial height was set to 1000 μm for 800–1200 L min^{-1}, 800 μm for 1400 L min^{-1}, and 600 μm for 1600 L min^{-1}. These heights were selected based on the maximum heights typically seen for each air flow rate; excessive height exacerbates the issues with out-of-plane features (as well as increasing processing time); a height too small may miss film. The results of this step are shown in the top image of Fig. 3.
2. *Axial blur.* Images were blurred in the axial direction across five rows to reduce the number of single-pixel errors that occur in edge location. Little variation in film height is observed in the images at such short axial range. The results of this step are shown in the second image of Fig. 3.
3. *Median filter.* A median filter is then applied to remove single-pixel noise while preserving the interfacial edge. Median filters are a standard image processing step to remove single-pixel noise. They are appropriate when the physical scale of measurements is much larger than the pixel size, as is the case for these PLIF data. To minimize the blurring effect of this filter, a neighborhood size of 3 pixels in both directions (minimum size possible) was used. The result of this step appears as the third image from the top in Fig. 3. In general, this image is the best for manual image investigation; it was saved for later use.
4. *Row-by-row stretch.* The image then undergoes a histogram adjustment and a linear stretch row-by-row to saturate low and high intensities. Areas of thinner film are less bright (since there is less height as well as less distance into the plane of image from which fluorescence occurs). This produces similar intensities for an entire image, regardless of intra-image height variations and ensures a smoother edge is detected.
5. *Morphological open/close.* The resulting image is then morphologically opened and then closed, which was found to significantly reduce the effects of single-pixel noise in the final edges.
6. *Median filter.* A second median filter, again with a neighborhood size of 3 pixels in both direction, is then used (fourth image from the top in Fig. 3).
7. *Threshold and erosion.* The portions of the resulting image brighter than a specified intensity threshold (200) are located and subjected to an image erosion. The edges located in this step are superimposed on top of the third image shown in Fig. 3, the results of which are the fifth image in Fig. 3. A threshold operation is required to identify the areas occupied by the liquid phase. The erosion is used to identify only that area that represents the continuous film, rather than small areas of higher fluorescence intensity away from the film (e.g., droplets).
8. *Edge selection.* When multiple edges are found, that nearest the wall usually corresponds to the actual gas–liquid interface. This edge is identified for each row and placed into a vector. Edges located within 40 μm are excluded (near-wall distortion region). The selected edges are indicated in the sixth image in Fig. 3.
9. *1-D median filter.* A one-dimensional median filter with a radius of 11 pixels is applied to the edge vector to remove single-pixel noise that manifests as single row errors (seventh image in Fig. 3). Since the film height varies slowly with axial distance, this filter ensures a better match to a smooth line.
10. *Accounting for bubbles.* A bubble reduction algorithm is employed only for images less than 300 μm in average film thickness (base film and small waves). This removes approximately 30–50% of the spurious results due to bubbles (see eighth image in Fig. 3). Spurious edges due to bubbles average 100 μm in length and appear as a depressions of approximately 30 μm in the film height. When a such a region is found (specifically, a segment of the edge 150 μm long that includes a mean depression of at least 15 μm relative to the surrounding film height), a linear interpolation between the two axial ends of the region replaces the original film edge detected.
11. *Outlier removal.* Outlier pixels within images are then excluded from analysis; these are generally out-of-plane features and spurious results.
12. *Height iterations.* Once these results are obtained, the height of the image is then adjusted and the process repeated until convergence (to within 20 μm or after 10 iterations) to address out-of-plane features that lead to over-prediction of film height. Each revision into the height considers the distribution of film heights within the image and the previous image height. The final image is shown as the bottom (ninth) image of Fig. 3.

Several of the processing steps include parameters that can be adjusted (e.g., the threshold used, the radius of filters). It is not

clear *a priori* to what values these should be set. However, it is expected that a correctly-identified edge will be a smooth, unbroken line across the image. Parameters should be selected to best approximate this goal.

An optimization process was used based on manual examination of selected images from a range of flow conditions as well as a calculation of edge smoothness, defined as follows. When adjacent rows both contain detected edges, the difference between the edge locations is taken to the power of 1.5, with all of these results summed for each image. Values such as the threshold, the size of bubbles to remove, and the like were set to minimize this metric (i.e., produce an edge with the fewest sudden jumps).

3.2. PLIF data analysis

The first step in processing the resulting edge data is to account for the slight imprecision in alignment. The wall location at the top of the image is found to be 6 pixels (19 μm) to the right of that at

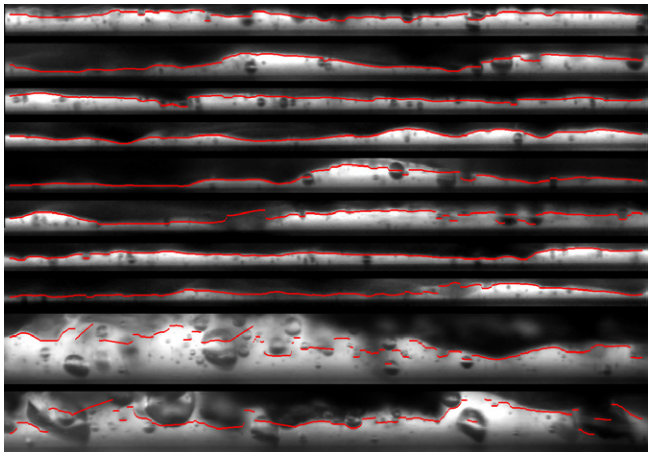

Fig. 4. Example processed images for example flow (U_{sg} = 55.3 m s^{-1}, U_{sl} = 12.7 cm s^{-1}). Flow is right to left.

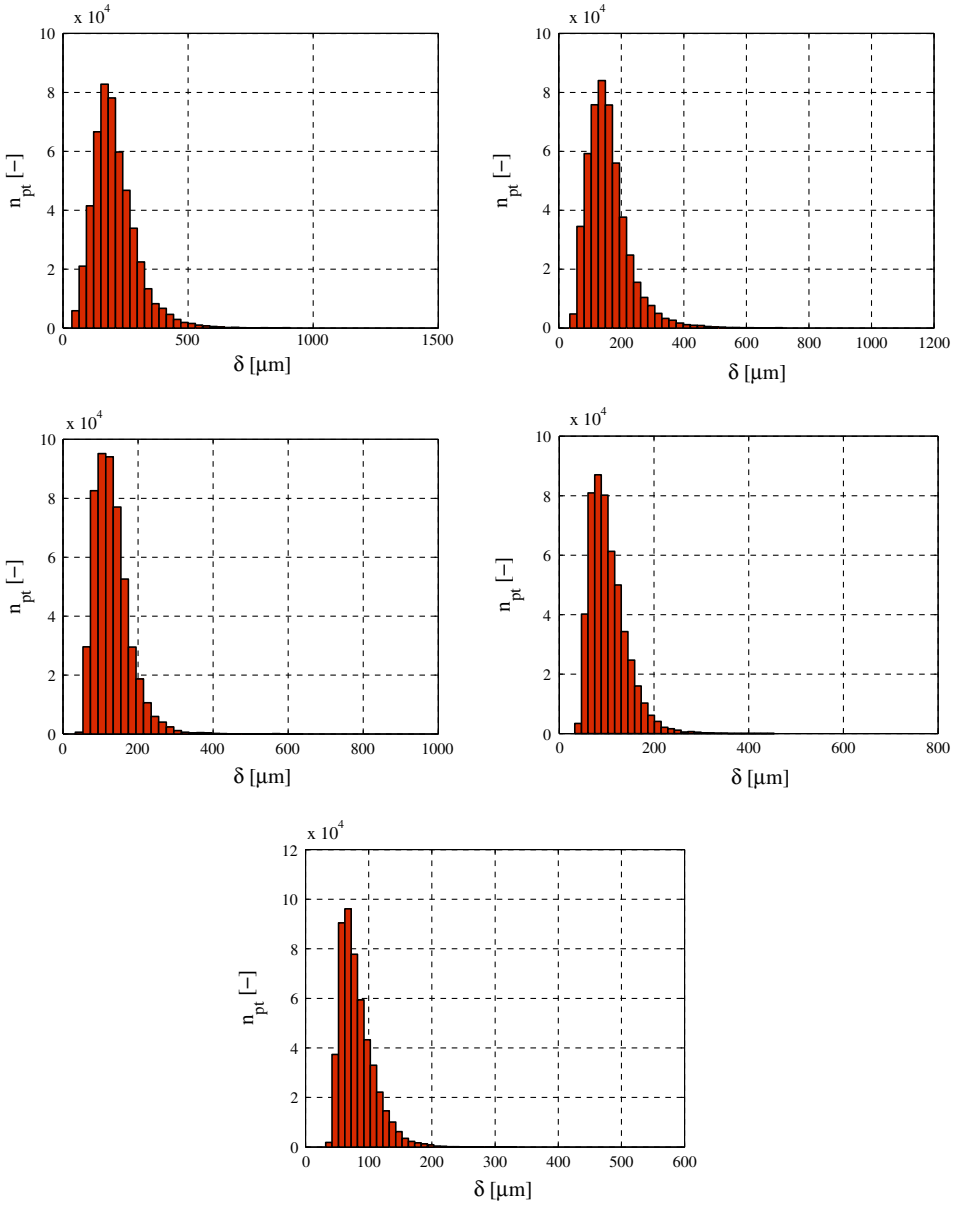

Fig. 5. Film thickness distributions, U_{sl} = 13 cm s^{-1}. U_{sg} = (*top left*) 36 m s^{-1}, (*top right*) 45 m s^{-1}, (*middle left*) 55 m s^{-1}, (*middle right*) 65 m s^{-1}, (*bottom*) 76 m s^{-1}.

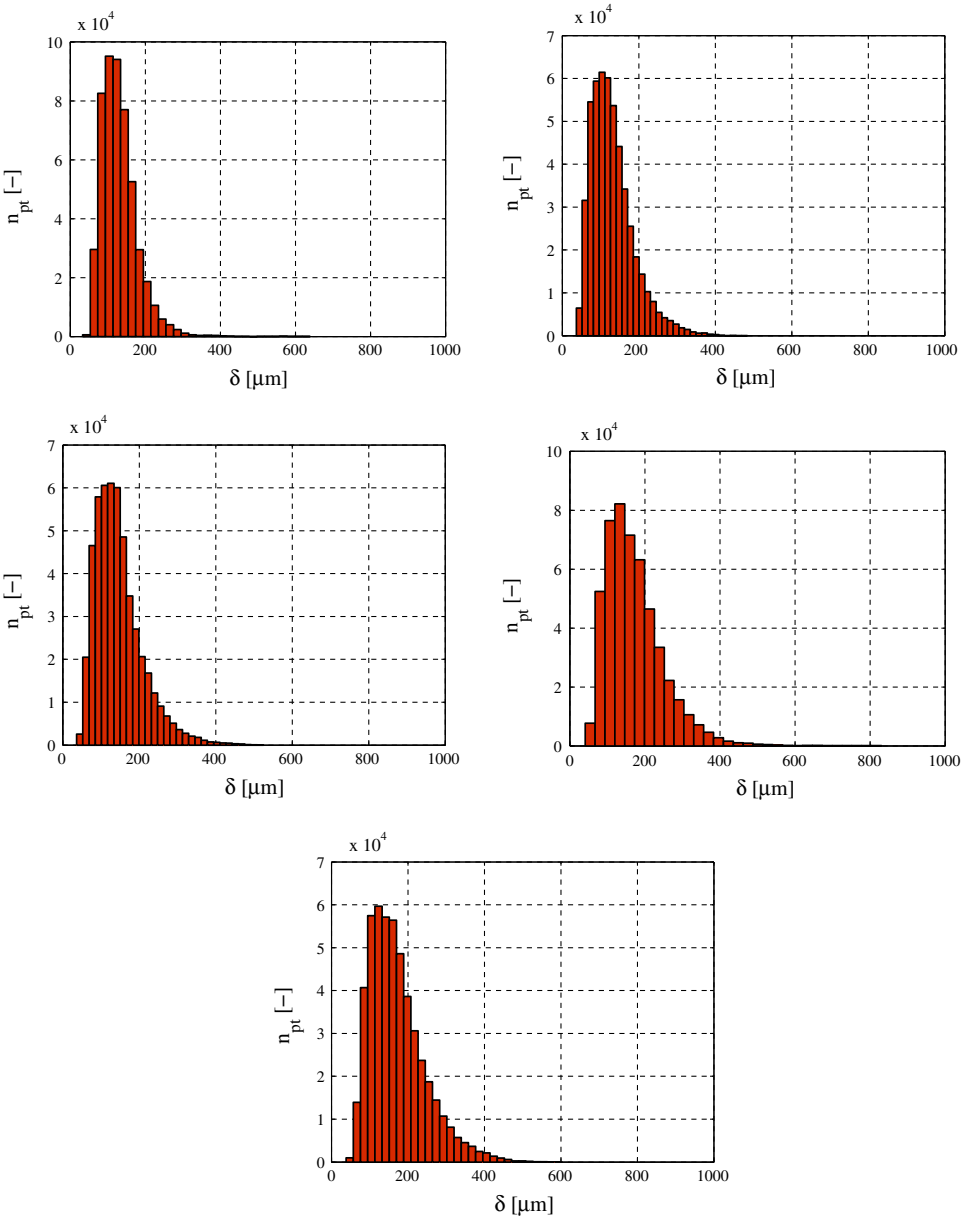

Fig. 6. Film thickness distributions, $Q_{g,nom}$ = 1200 L min^{-1} (U_{sg} = 54–60 m s^{-1}). U_{sl} = (*top left*) 6 cm s^{-1}, (*top right*) 13 cm s^{-1}, (*middle left*) 21 cm s^{-1}, (*middle right*) 30 cm s^{-1}, (*bottom*) 34 cm s^{-1}.

the bottom. The results from the image processing code are converted to physical coordinates with a linear adjustment for this misalignment.

Several figures are then generated. Spatial correlations across 100 μm, 200 μm, 500 μm, 1 mm, 2 mm, and 3 mm are shown. A histogram of film heights is also produced. The average film thickness of both images of a pair is also compared. For the correlations (spatial and image pair) considered, a linear regression is performed. The correlation coefficients (ρ_{corr}) are also output.

3.3. Examples of processed images

Ten images (U_{sg} of 55.3 m s^{-1} and U_{sl} of 12.7 cm s^{-1}) have been selected to provide examples of the processing algorithm, including wave and base film images for which the processing has varying degrees of success. The images are shown in Fig. 4.

Perhaps the most obvious feature of these processed images is the significant variation in image height due to the iterative procedure. The significant axial variations in brightness and its link to local film thickness are also immediately apparent, particularly for those images that include wide variation in film thickness.

Much of the processing code is designed to reduce the effects of bubbles on the estimate of interfacial location. Some bubbles that are imaged are in-plane features, actual perturbations of the interface. However, out-of-plane bubbles are likely more frequent since the radius of the tube is many times larger than the film thickness. Despite these efforts, not all bubbles are successfully avoided.

Consider, for example, the sixth image from the top of Fig. 4. Approximately 10 bubbles are found within the film; most of these do not affect the results. However, approximately 80% of the way from left to right, two large bubbles near one another obscure the actual interface. These bubbles appear somewhat out of focus; at least one is likely an out-of-plane feature. In this image, the right-most large bubble also caused difficulty.

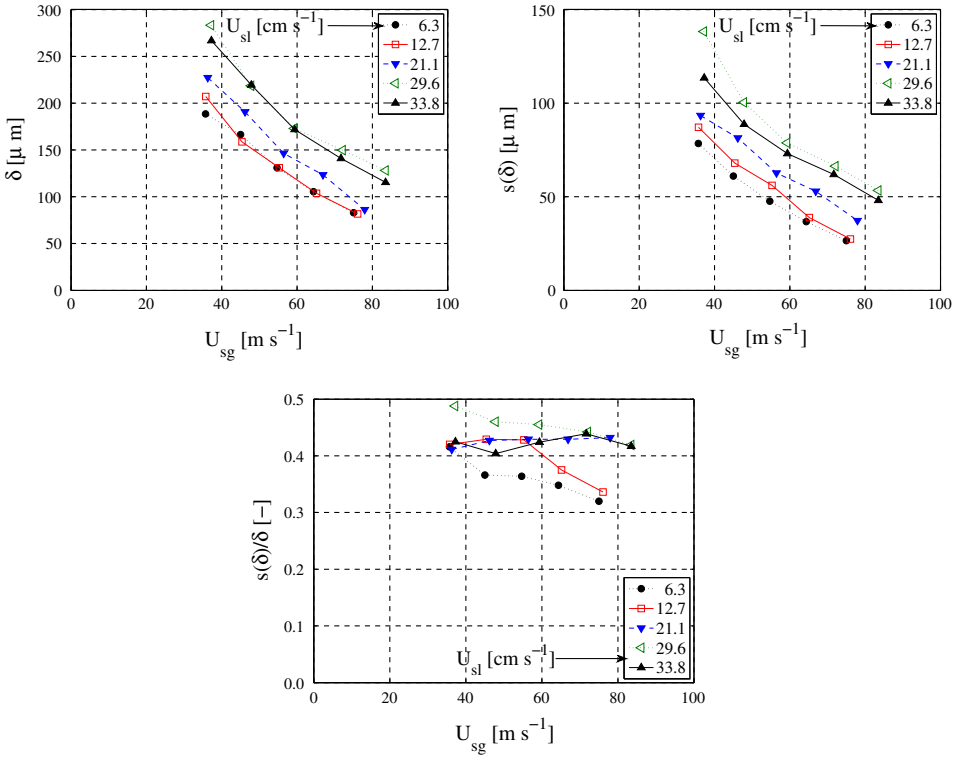

Fig. 7. (*Top left*) Average film thickness. (*Top right*) Average film roughness (standard deviation of film thickness). (*Bottom*) Ratio of film roughness to average film thickness.

The two widest example images, 9 and 10, demonstrate the additional difficulties of identifying the interface in waves, respectively. In image 10, the wave appears to be successfully found; the blurry bubbles at left are almost certainly out-of-plane features. In contrast, the film edge in image 9 is more poorly identified, as the combination of significant surface roughness and entrained bubbles yields poor interfacial tracking. Nonetheless, the mean film thickness found for this image appears reasonable.

Despite the difficulties noted in a number of these images, it appears that the code provides the location of the film to within 10 μm for approximately 95% of locations. At higher liquid flows and either extreme of gas flows, some of these problems are exacerbated, but a tracking rate of 90% is maintained (i.e., the code is accurate to within a few pixels 90% or more of the time).

3.4. Quantitative uncertainty analysis

The uncertainty on average film thickness is dominated by several bias uncertainties. The first is the location of the wall, determined manually for each "set" of data (usually, a series of constant U_{sl}). A set of data was taken in a single session, without a complete shut down of the loop. These shut downs necessitated camera focus adjustment and shifted the location of the wall by up to 30 μm. The uncertainty between sets (and between a given set and the actual wall location) is estimated as 3 pixels (10 μm). Since this uncertainty would move the entirety of the results from a flow condition up or down uniformly, no effect on roughness data is present.

The second type of uncertainty is due to the processing of the images. Procedures such as crop heights, median filter radii, axial blur radius, and the threshold used for edge detection each require manually-selected parameters. The sensitivity of the average and standard deviation of film heights on these parameters was explored.

The strongest effect on average film thickness (approximately 5–10 μm) is due to the threshold used in the edge detection, which is itself rooted in diffraction and the finite depth of field and laser sheet thickness. Based on the optics discussed above, a diffraction-limited resolution on a point of 15 μm is estimated. However, the images are of an area, with the edge of the area of particular interest, and undergo considerable processing prior to edge identification. This edge appears somewhat burred; this is likely rooted in diffraction and the finite laser sheet thickness. The threshold in edge detection was set to 200 (out of 255 maximum – this operation was performed on an 8-bit version of the image), based on manual examination of images and the code's metric pertaining to the smoothness of the edge detected. This uncertainty is estimated at 5–10 μm based on the range of average film thicknesses obtained for threshold values that produced qualitatively reasonable results (i.e., smooth lines near the visually-identified interface in selected images).

In total, these "global" image processing procedures (i.e., all those not specifically targeted at bubbles/droplets) have an associated uncertainty of 10 μm on the average and 5 μm on the roughness. The uncertainty on roughness is smaller, since many of these parameters tend to increase or decrease estimated film heights throughout all images in a positively correlated way. (For example, an increased threshold would decrease film height estimates, but have little effect on roughness estimates.)

Another area of concern are the procedures to account for the effects of bubbles and out-of-plane features (such as droplets). The images for the flow condition shown in Fig. 4 have been examined in detail. On average, slightly less than one bubble is "missed" (i.e., film location under-estimated) per image. The average inaccuracy is approximately 40 μm (radial); the average extent of the mis-identified line is 75 μm (axial). This contributes a bias error of 2–3 μm (underprediction). In addition, approximately 1 out-of-plane feature above the film is mis-identified in every 10 images; the average inaccuracy is 150 μm for 200 μm. This leads

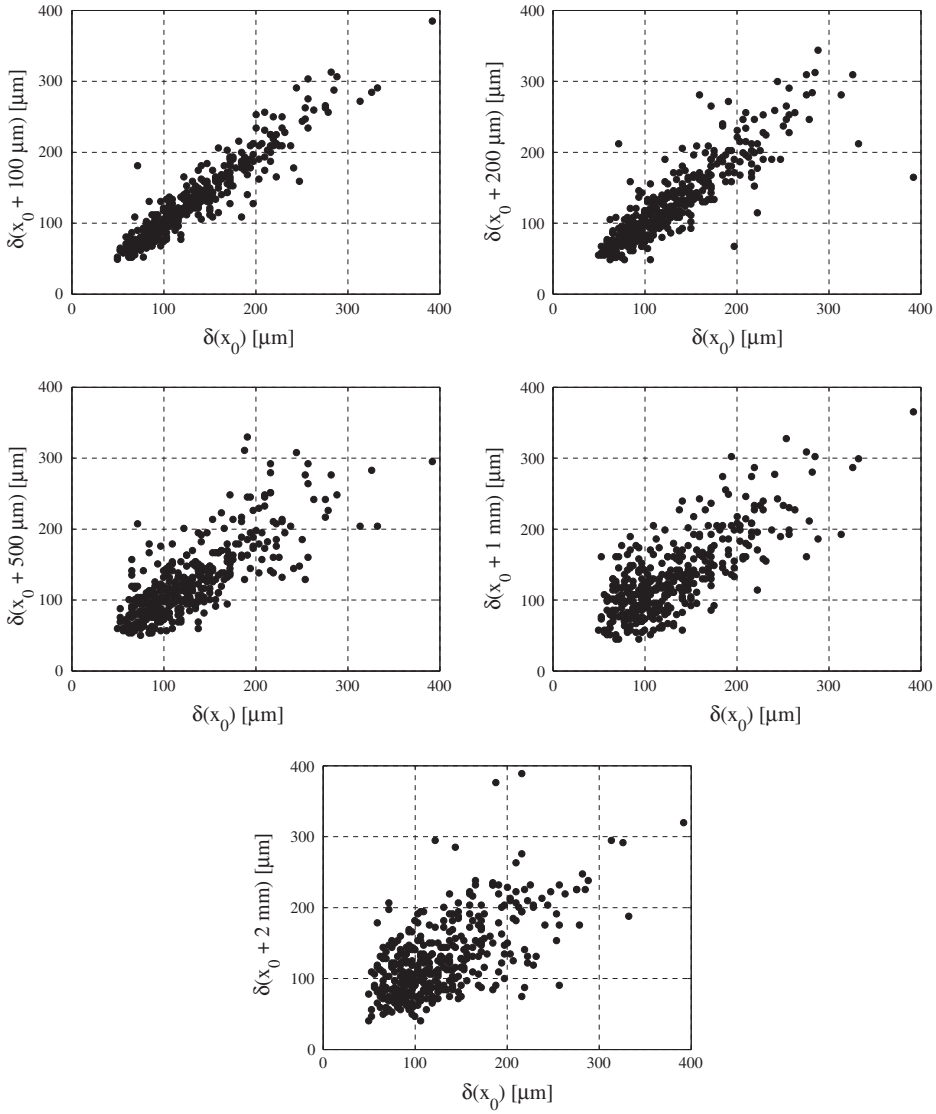

Fig. 8. Spatial correlations for example flow (U_{sg} = 55.3 m s^{-1}, U_{sl} = 12.7 cm s^{-1}). Δx = (*top left*) 100 μm, (*top right*) 200 μm, (*middle left*) 500 μm, (*middle right*) 1 mm, (*bottom*) 2 mm.

to a systematic over-prediction of 2–3 μm. Therefore, it is expected that the net effect on the average film thickness of the imperfect assessment of bubbles/out-of-plane features is small; however, this may bias the estimate of roughness (standard deviation) upward by up to 5 μm.

The statistical uncertainty (95% confidence), assuming 400 degrees of freedom (equal to the number of images), on the average film thickness is estimated at 10 μm, based on an average roughness of 62 μm. Since this statistical uncertainty is small – on the same order of the processing uncertainty – 400 images is sufficient and little gain in accuracy will be achieved with more images.

The total uncertainty for the average film thickness can therefore be estimated at 25 μm relative to the actual value or between sets and 15 μm within a set, as the wall location bias does not apply within a set (data acquired in single session). The standard deviations are also of interest as estimates of roughness. Additional fractional uncertainty is noted at larger gas flows, due to an increased fraction of large waves being spurious results. An uncertainty on total film roughness of 10 μm is estimated.

4. PLIF results

Example film thickness distributions and spatial correlations are discussed in this section. The full set of graphs are available in the electronic annex to this article.

4.1. Film thickness distributions

Selected film thickness distributions are shown in Fig. 5 (constant U_{sl}) and Fig. 6 (similar U_{sg}, constant $Q_{g,nom}$). The shape of these distributions is similar across a wide range of flow conditions, although the absolute film heights change significantly.

The bulk of the film thickness measurements occur in a sharp peak, well below the maximum film thickness detected. These are predominantly base film. To the right of the peak are wave height results. The peak is not symmetric (positive skew). Additional skew can be seen with increasing liquid flow in Fig. 6, likely linked to the additional disturbance wave activity at high U_{sl}. Another form of asymmetry is also detected for the highest gas flows in Fig. 5, with the left edge appearing somewhat clipped. This is

likely rooted in the minimum detectable film thickness (near-wall distortion region). Some film thickness trends can be observed directly from the distributions. Both the average and width of the distribution increase with increasing liquid flow and decrease with increasing gas flow. These results are shown in Fig. 7.

The third plot in Fig. 7 shows the ratio of roughness, taken as the sample standard deviation of all film thickness data, $s(\delta)$, to average film thickness. This ratio is not constant for the all annular flow conditions investigated, as is implicitly assumed in many film roughness correlations for interfacial shear. At sufficient liquid flow (U_{sl} above 15 cm s^{-1} for the conditions of these tests), a ratio of approximately 0.4 is seen with good consistency. At lower liquid flows (especially at high gas flow), the ratio is smaller. This may be linked to the decreased prominence of disturbance waves for these flow conditions. In Part II: Analysis and Comparison to Models (Schubring et al., 2010), information from Schubring et al. (2010) is integrated with these PLIF data to separate effects of base film and waves.

4.2. Spatial correlations

Plots of spatial correlations are shown in Fig. 8 for the flow with U_{sg} of 55.3 m s^{-1} and U_{sl} of 12.7 cm s^{-1}. In these plots, x_0 (a fixed axial location for the consideration of axial variations) is selected to be 50 pixels (157 μm) from the bottom of the image. The trends discussed presently occur for all x_0 locations tested. To provide the best view of the most film thickness results, a small number of the largest wave heights are beyond the axes shown on these plots. All film thickness results are considered in the calculation of the linear correlation coefficients, ρ_{corr}.

At short axial distances, film thickness varies little relative to its global variation. For the flow shown in Fig. 8, ρ_{corr} at 100 μm is 0.947. At 200 μm, 500 μm, 1 mm, and 2 mm, this reduces to 0.850, 0.789, 0.733, and 0.618, respectively. At short ranges, all flows show strong correlation. As the range extends to 2 mm, the correlation coefficients drop, with low liquid and high gas flows becoming less correlated more quickly. These conditions are most likely to show wave and base film behavior in the same image, reducing ρ_{corr} when base film and wave portions are compared. Work with a 6.5 μm pixel size (8 mm axial length) indicated that the trends in ρ_{corr} with axial distance continue to larger separations.

5. Conclusions

- Planar laser-induced fluorescence (PLIF) has been applied to vertical air–water annular flow to provide direct visualization of the thin liquid film.
- A machine vision solution for gas–liquid interface detection on these images has been devised, allowing for the estimation of film thickness distribution.
- The shape of the film thickness distribution, characterized by an asymmetric peak (positive skew), is similar across a wide range of gas and liquid flow rates (although the absolute heights of the film vary). This skew is indicative of the distinction between base film and waves and is more pronounced at high U_{sl}.
- Average film thickness and the standard deviation of film thickness decrease with gas flow and increase with liquid flow; the effects with gas flow are stronger.
- At sufficient U_{sl}, the standard deviation is approximately 40% of the average film thickness, with low liquid flows displaying a smaller fractional roughness.

The images themselves indicate that at the spatial scales shown (4 mm axial direction), the roughness in annular flow is not homogeneous as often assumed in modeling. Indeed, most images show exclusively wave behavior or exclusively base film behavior; single-zone images are particularly dominant at high liquid flow rates.

Further consideration of base film and wave behavior and application of these film roughness data to annular flow modeling are discussed in Part II: Analysis and Comparison to Models (Schubring et al., 2010).

Acknowledgement

The financial support of Bettis Laboratory is gratefully acknowledged.

References

Asali, J.C., Hanratty, T.J., Andreussi, P., 1985. Interfacial drag and film height for vertical annular flow. AIChE J. 31, 895–902.
Brown, R.C., Andruessi, P., Zanelli, S., 1978. The use of wire probes for the measurement of liquid film thickness in annular gas–liquid flows. Can. J. Chem. Eng. 56, 754–757.
Clark, W.W., 2002. Liquid film thickness measurement. Multiphase Sci. Technol. 14, 1–74.
Fore, L.B., Beus, S.G., Bauer, R.C., 2000. Interfacial friction in gas–liquid annular flow: analogies to full and transition roughness. Int. J. Multiphase Flow 26, 1755–1769.
Fossa, M., 1998. Design and performance of a conductance probe for measuring the liquid fraction in two-phase gas–liquid flows. Flow Measur. Instrum. 9, 103–109.
Hewitt, G.F., Hall Taylor, N.S., 1970. Annular Two-Phase Flow. Pergamon Press, Oxford, UK.
Hewitt, G.F., Jayanti, S., Hope, C.B., 1990. Structure of thin liquid films in gas–liquid horizontal flow. Int. J. Multiphase Flow 16, 951–957.
Hurlburt, E.T., Fore, L.B., Bauer, R.C., 2006. A two zone interfacial shear stress and liquid film velocity model for vertical annular two-phase flow. In: Proceedings of the ASME Fluids Engineering Division Summer Meeting 2006, vol. 2, Miami, FL, USA, pp. 677–684.
Ishii, M., Mishima, K., 1981. Correlation for liquid entrainment in annular two-phase flow of low viscous fluid. Argonne National Laboratory Report ANL/RA/LWR 81-2.
Kataoka, I., Ishii, M., Nakayama, A., 2000. Entrainment and deposition rates of droplets in annular two-phase flow. Int. J. Heat Mass Transfer 43, 1573–1589.
Kishore, B.N., Jayanti, S., 2004. A multidimensional model for annular gas–liquid flow. Chem. Eng. Sci. 59, 3577–3589.
Owen, D.G., Hewitt, G.F., 1987. An improved annular two-phase flow model. In: 3rd International Conference on Multi-Phase Flow, The Hague, Netherlands, pp. 73–84.
Rodríguez, D.J., Shedd, T.A., 2004. Cross-sectional imaging of the liquid film in horizontal two-phase annular flow. In: 2004 ASME Heat Transfer/Fluids Engineering Summer Conference, Charlotte, NC. Paper 56445.
Rodríguez, D.J., 2004. Characterization of bubble entrainment, interfacial roughness and the sliding bubble mechanism in horizontal annular flow. PhD thesis, University of Wisconsin-Madison, Madison, WI, USA.
Schubring, D., Shedd, T.A., 2008. Prediction of wall shear for horizontal annular air–water flow. Int. J. Heat Mass Transfer 52, 200–209.
Schubring, D., Shedd, T.A., Hurlburt, E.T., 2010. Studying disturbance waves in vertical annular flow with high-speed video. Int. J. Multiphase Flow 36, 385–396.
Schubring, D., Shedd, T.A., Hurlburt, E.T., 2010. Planar laser-induced fluorescence (PLIF) measurements of liquid film thickness in annular flow. Part II: interpretation and modeling. Int. J. Multiphase Flow 36, 825–835.
Wallis, G.B., 1969. One-Dimensional Two-Phase Flow. McGraw-Hill Inc., New York, NY, USA.
Wolf, A., Jayanti, S., Hewitt, G.F., 2001. Flow development in vertical annular flow. Chem. Eng. Sci. 56, 3221–3235.